Transactions of the Korean Nuclear Society Autumn Meeting
Gyeongju, Korea, October 29-30, 2026

CFD Analysis of Two-Phase Flow Instability in a Passive Containment Cooling System

Yong Kab Lee [a] , Jong Chull Jo [b*],
[a] *SIMEX, 173 Digital-ro, Geumcheon-gu, Seoul, 08511*
[b] *TIUM solutions, 233 Dogok-ro, Gangnam-gu, Seoul, 06230*
[*] *Corresponding author: jcjo@tiumsolutions.com*

Keywords : passive containment cooling system, CFD analysis model, two-phase flow instability, geysering

1. Introduction

The passive containment cooling system (PCCS) of the innovative Small Modular Reactor (i-SMR) limits the peak pressure in the steel containment vessel (CV) after design-basis accidents and maintains containment integrity for 24 hours without operator action or AC power [1]. Steam released into the CV condenses on the PCCHX tubes, and the condensation heat transferred to the tube-side water drives natural convection and then boiling, establishing natural circulation between the PCCHX and the emergency cooling tank (ECT) [1].

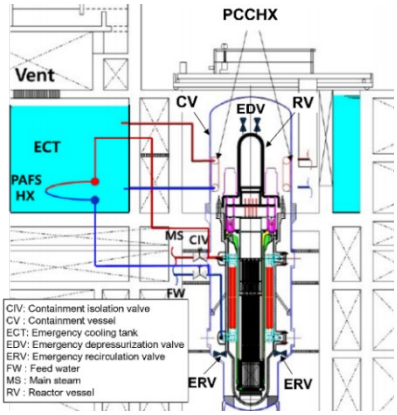


Fig.1 Schematic of the PCCS for the i-SMR [1].

Because the driving head arises solely from the density difference between the two-phase riser and the single-phase downcomer, it is inherently small and the system is susceptible to two-phase flow instability that may degrade the cooling performance of the PCCS [2]. Among the reported mechanisms [2-6], geysering is of particular concern at the low pressure of the limiting ECT condition: boiling in the heated riser expels the overlying liquid column, which is replaced by cooler upstream liquid that is reheated to boiling, and the cycle repeats.

A numerical model able to reproduce these oscillations is useful for independent regulatory confirmation of separate-effect test results submitted in support of the PCCS passive cooling performance. This study develops a CFD model of the simplified square loop of Fig.2 in order to (a) identify the threshold heat input triggering geysering-type oscillations, (b) characterize the amplitude dependence on heat input within the credible range, (c) establish that range with respect to the critical heat flux (CHF) limit, and (d) quantify the discrepancy against a one-dimensional drift-flux bulk model.

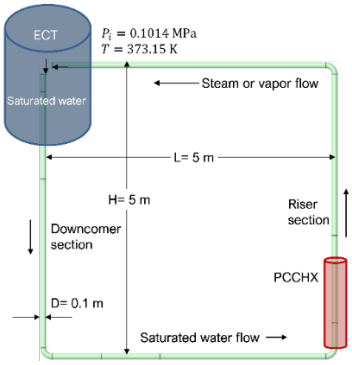


Fig.2 CFD analysis model of the PCCS.

2. Methods and Results

2.1 Problem Statement

The geometry and operating conditions of the PCCS model considered in this analysis are given in Table 1.

Table 1. Geometry and operating conditions

Item	Symbol	Value
Pipe inner diameter	D	0.1 m
Loop height	H	5 m
Loop width	L	5 m
Heated span length	L_h	1.5 m
Heated pipe thickness	L_t	0.005 m
Heated span location	-	bottom of the riser
ECT pressure	p	0.1014 MPa
ECT temperature	T_{sat}t	373.15 K (saturated)
Inlet subcooling	ΔT_{sub}	0 K
Heat input range	$\dot{q}$	10 - 100 kW

The model represents the limiting ECT condition, in which the ECT coolant has reached saturation at atmospheric pressure so that the subcooling available to suppress boiling is essentially zero. Saturated water flows from the ECT into the downcomer by gravity, passes through the lower horizontal pipe, is heated over the 1.5 m PCCHX span at the bottom of the riser, rises as a two-phase mixture and returns to the ECT through the upper horizontal pipe. The loop inlet and outlet are submerged in the ECT water at the same elevation, so their static heads cancel exactly and the circulation is driven exclusively by the riser-to-downcomer density difference. Because the inlet subcooling is zero, boiling begins in the heated span at any non-zero heat input, and the 10-100 kW range examined is that planned for the separate-effect test of the i-SMR PCCS on a test loop of the same configuration; within it, the sub-range credited for interpretation is fixed by the closure-validity criterion of Section 2.3.

2.2 CFD Analysis

Governing equations for the steady-state two-phase flow including boiling and conjugate heat transfer in the PCCHX tube are solved with ANSYS-CFX [7], the walls being no-slip and adiabatic except over the heated span, with a separate calculation for each of the heat inputs of 10, 30, 40, 50, 60, 70 and 100 kW. The Eulerian multiphase model is applied with the SST model for the liquid and the disperse zero equation model for the vapor, and phase change is calculated with the bulk boiling model. Drag, turbulent dispersion and turbulence transfer employ the Ishii-Zuber, Lopez de Bertodano and Sato enhanced eddy viscosity models [8]. The loop outlet is an opening boundary at the ECT hydrostatic pressure with saturated liquid at 373.15 K returning to the loop.

A hexahedral mesh is adopted for the flow field and the heated wall, with inflation layers giving y+ < 1 from 20 boundary-layer elements. Mesh convergence tests on the calculated flowrate $\dot{m}$ for grids of about 1 to 3 million elements led to the adoption of a 1.86 million element mesh.

The steady-state solution is obtained by time-step marching iteration, and two behaviors are observed. Where a stable steady solution exists the monitored flowrate passes through an initial numerical transient, which belongs to the iteration procedure and not to the physics and is excluded from the comparison, and then converges. Where none exists the flowrate settles into a sustained oscillation of constant amplitude that does not decay with further iteration.

2.3 Analysis Results and Discussions

Fig.3 shows the calculated void fraction contours at two heat inputs. In both cases boiling occurs in the heated span and a thermally stratified mixture forms in the upper horizontal pipe.

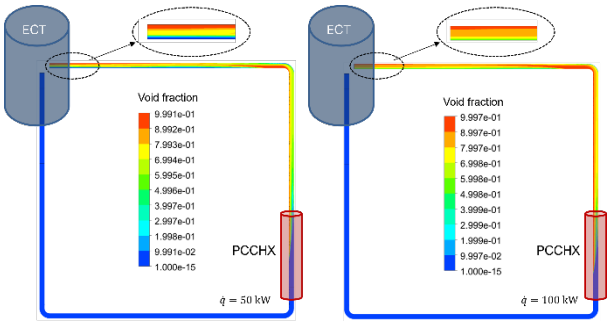


Fig. 3 Void fraction contours for $\dot{q} = 50$ and 100 [kW].

The riser differs markedly: the vapor is dispersed and intermittent at the lower heat input, characteristic of the slug-churn regime, whereas at the higher one it forms a nearly continuous annular core.

Table 2 gives the calculated mass flowrate $\dot{m}$, the peak-to-peak amplitude of its oscillation, the area-averaged void fraction $\bar{\alpha}$ at the loop exit, the maximum void fraction $\alpha_{\max}$ at the heated inner wall, and the one-dimensional drift-flux flowrate $\dot{m}_{1D}$ of Section 2.3 (last row).

Current CFD boiling closures are formulated for the nucleate boiling regime and lose validity as the heated wall approaches the CHF condition, a void fraction near 0.9 being commonly taken as an indicator of that approach [8-10]. The indicator must, however, be applied on the basis for which the closures are written: the Ishii-Zuber, Sato and Lopez de Bertodano relations are constitutive models for cross-sectionally averaged flow regimes, whereas $\alpha_{\max}$ is a resolved outcome of the calculation and not a measure of its validity; applied to it the 0.9 threshold would invalidate every case above 10 kW and so be vacuous. The credible range is therefore delimited by the area-averaged exit void fraction, which characterizes the bulk regime the closures represent, while $\alpha_{\max}$ is retained in Table 2 only as an uncertainty qualifier for proximity to CHF.

Table 2. CFD calculation results

$\dot{q}$ [kW]	**10**	**30**	**40**	**50**	**60**	**70**	**100**
$\dot{m}$ [kg/s]	9.81	12.84	13.14	13.25	13.04	12.75	11.62
Amplitude of $\dot{m}$	0.0	0.0	0.0	2.248	1.469	0.0	0.0
$\bar{\alpha}$ at exit	0.42	0.63	0.69	0.73	0.77	0.80	0.86
α_{max}@heated wall	0.794	0.917	0.935	0.944	0.955	0.960	0.971
$\dot{m}_{1D}$ [kg/s]	10.05	12.76	13.40	13.87	14.22	14.51	15.10

A further condition controls where boiling begins. Because the heated span lies well below the ECT free surface, the static head raises the local saturation temperature T_{sat}, so that water leaving the saturated ECT enters the span subcooled; removing that subcooling would demand more heat than any input examined here. The present calculations prescribe the saturation temperature at its atmospheric value, which promotes boiling and so gives the conservative condition sought here but does not represent this elevation-induced subcooling; evaluating the saturation temperature from the local pressure, which would delay the onset of boiling, is recommended for practical simulations. For reference, the wall heat flux over the heated span is

$$q'' = \dot{q}/(\pi\, D\, L_h) \qquad (1)$$

which remains, over the range examined, well below the Zuber pool-boiling CHF [11] at the same pressure,

$$q''_{CHF} = 0.131 {\rho_v}^{1/2}\, h_{lv}\, [\sigma_s\, g\, (\rho_l - \rho_v)]^{1/4} \qquad (2)$$

The two are not in conflict: Eq. (2) limits low-quality high-flux boiling by departure from nucleate boiling, whereas at the void fractions reached here the flow is annular and the limiting phenomenon is dryout of the wall liquid film, which occurs at a far lower heat flux. The void fraction criterion therefore governs, the Zuber value serving only as an upper bound. On this basis the area-averaged exit void fraction indicates departure from the bulk boiling regime at the upper end of the range examined, so the highest heat inputs are not credited.

Within the credible range $\bar{\alpha}$ increases monotonically with heat input while $\dot{m}$ passes through a maximum near 50 kW. That maximum is a property of the natural-circulation balance and not a numerical artefact. Driving head and resistance both depend on the heat input through the phase-change number $N = x_e[(\rho_l/\rho_v) - 1]$,

$x_e = q/\dot{m}h_{\mathrm{lv}}$. On a homogeneous basis $\alpha_e = N/(1+N)$, which reproduces the exit void fractions of Table 2 to two decimals over the whole range, $\bar{\alpha} = C_a\alpha_e$ with $C_a = 0.88-0.94$, and $\Phi_{\mathrm{lo}}{}^2 = 1+N$ gives $K_{\mathrm{eff}} = K_0(1+BN)$, so that the balance yields

$$\dot{m} = A\sqrt{C\,f(N)},\ f(N) = N/[(1+N)(1+BN)] \quad (3)$$

with $C = [2\rho_l gH(\rho_l-\rho_v)C_a]/K_0$. The driving factor $N/(1+N)$ saturates at unity, since the riser cannot become less dense than pure vapor, whereas $1/(1+BN)$ decreases without bound, so their product has an interior maximum at $N^* = 1/\sqrt{B}$. The observed maximum at 50 kW gives $N = 2.68$ and hence $B = 0.14$, consistent with the loss distribution of the loop. It occurs at so low a power because of the low pressure: $(\rho_l/\rho_v)-1$ is 1601 at 0.1014 MPa against 4.83 at 15.5 MPa. At and below 40 kW the iteration converges to a constant flowrate and no oscillation is present; above a threshold lying between 40 and 50 kW a sustained oscillation is established, and resolving it more finely is recommended for test planning.

The oscillation modulates the flowrate without interrupting it, the instantaneous value remaining close to the time-mean throughout. Only two oscillatory points fall within the credible range and the amplitude does not grow monotonically between them, so no trend of amplitude with heat input can be established.

The flowrates were also compared with a one-dimensional bulk analysis of the same loop using the drift-flux correlation [12] ($C_0 = 1.2, V_{\mathrm{gj}} = 0.24$ m/s) with the void fraction integrated over the heated span and the riser and K_0 taken from the CFD at the flowrate maximum, so that the comparison isolates the void and friction modelling. In the last row of Table 2 the bulk model matches the CFD to within about 2% at 10 kW and a few percent up to 50 kW, but over-predicts by 14% at 70 kW and 30% at 100 kW and rises monotonically, so it does not reproduce the maximum. Three omissions account for the growth: a single cross-sectional void fraction in place of the wall-peaked distribution raises the effective driving head through C_a, while the homogeneous treatment of the stratified return leg and the liquid-only friction factor with the acceleration pressure drop neglected both lower B in Eq. (3). All three scale with N, so the over-prediction necessarily grows with heat input.

Fig.4 plots the monitored flowrate at the downcomer inlet against the accumulated time steps, the initial numerical transient being discarded. Because the calculation is a steady-state formulation advancing in pseudo-time, the abscissa is not physical time: the non-decaying oscillation establishes only that no steady-state solution exists at that heat input, that is, the onset of instability, and yields neither frequency, period nor amplitude, which require a transient calculation. The oscillation is identified as the geysering type not from the pseudo-time signal but by cross-validation with the intermittent slug-churn void fraction distribution of Fig. 3 and with the closed-form flashing model of Ref. [13] discussed below.

As shown in Table 2 and Fig.4, a sustained oscillation of $\dot{m}$ appears once $\dot{q}$ exceeds the threshold identified above. This is compared below with the closed-form solution for the flashing-induced transient boiling interface level z(t) in a PCCS [13].

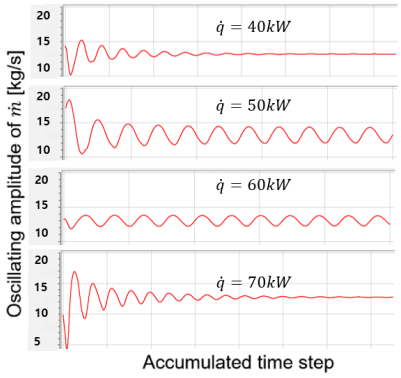


Fig. 4 Effects of $\dot{q}$ on $\dot{m}$.

The non-linear equation for the boiling interface level z derived in reference [13] is solved by the perturbation method with

$$z = z_o + \epsilon z_1 + \cdots \quad (4)$$

For the first-order perturbation ϵ^1, a second-order differential equation for the unsteady term $z_1(t)$ is derived as,

$$a\,\ddot{z_1} + b\,\dot{z_1} + c\,z_1 = 0 \quad (5)$$

whose solution, for an interface displaced from its steady level z_0 and released from rest, is

$$\frac{z_1(t)}{z_{10}} = e^{\sigma t}\left[cos(\omega\, t) - \frac{\sigma}{\omega}\, sin(\omega\, t)\right] \quad (6)$$

where

$$\sigma = -\frac{b}{2a} = \frac{(H+L)\,\dot{q}}{z_0\,A\,\Delta h\,\Lambda} \quad (7)$$

$$\omega = \sqrt{\omega_n{}^2 - \sigma^2}, \quad \omega_n{}^2 = \frac{g(\rho_l-\rho_v)}{\Lambda} \quad (8)$$

$$\Lambda = \rho_l(H+L+z_0) + \rho_v(H+L-z_0) \quad (9)$$

$$z_0 = H - \Sigma\,\Delta p_{KL}/[g(\rho_l-\rho_v)] \quad (10)$$

The coefficient σ of Eq. (7) is positive for any non-zero heat input, so the damping of the interface motion is negative and the oscillation term of Eq. (6) grows through the exponential factor. The growth rate increases with q and with decreasing loop pressure loss through z_0 in Eq. (10), and decreases with larger flow area or greater enthalpy change, so a non-zero heat input is always destabilizing in the linear sense. Equation (7) gives the growth rate of a linearized perturbation and not the limit-cycle amplitude reached by the CFD solution, so the two are not directly comparable.

In an actual accident sequence the heat load falls to a small fraction of its peak value within minutes, so the oscillatory behavior examined here is relevant mainly to the early transient and the constant-heat-input calculations are conservative in that respect.

Because σ is small over the range considered, $\sigma/\omega \ll 1$ and $\omega \simeq \omega_n$, so that $e^{\sigma t} \simeq 1$ over the times of interest. Equations (4) and (6) then reduce to

$$z(t) \simeq z_0 + \epsilon z_{10} \cos(\omega_n t) \quad (11)$$

Equation (11) describes a bounded oscillation of the interface about its steady level, qualitatively consistent with the bounded, non-decaying flowrate oscillations of Fig. 4. The correspondence is qualitative only since Eq. (11) refers to the interface level and Fig. 4 to the loop mass flowrate.

3. Conclusions

A CFD analysis of the geysering-type two-phase flow instability in a simplified square model of the i-SMR PCCS loop has been performed at the limiting ECT condition of saturated water at atmospheric pressure. Owing to the limitations of current CFD boiling closures, only the calculations within the range of validity of the bulk boiling model were credited.

Within that range the threshold heat input lies between 40 and 50 kW, consistent with the closed-form flashing model in which the growth rate of a linear perturbation is proportional to the heat input; that model predicts a growth rate rather than a limit-cycle amplitude, and the oscillatory points obtained are too few to establish how the amplitude varies with heat input. The oscillation does not hinder the natural circulation, the time-mean flowrate being maintained. The flowrate passes through a maximum near 50 kW, an intrinsic feature of the natural-circulation balance at low pressure and not a numerical artefact.

The bulk drift-flux model over-predicts the flowrate, increasingly so with heat input, and does not reproduce that maximum, so it is non-conservative for performance demonstration. The present results are a self-consistent numerical prediction not yet compared with measurement; validation against separate-effect test data, together with a boiling model valid through the annular and post-dryout regimes and a dryout-type CHF correlation, is required before the model is used to confirm PCCS cooling performance.

NOMENCLATURE

A = cross-sectional flow area of a circular pipe [m^2]
B, C, C_a = coefficients of the loop balance, Eq.(3)
a, b, c = coefficients of Eq.(5)
C_0, V_{gj} = drift-flux parameter [-] and drift velocity [m/s]
D, H, L = pipe inner diameter, loop height, and width [m]
g = acceleration of gravity [m/s^2]
h_{cl}, h_{lv} = sensible heat to saturation and latent heat [kJ/kg]
K_0, K_{eff}, K_L = loop loss coefficients, Eq.(3)
L_h, L_t = heated span length and pipe thickness [m]
$\dot{m}, \dot{m}_{1D}$ = mass flowrate, CFD and 1-D drift flux [kg/s]
N, N^* = phase-change number, its value at maximum flowrate
q = heat input [kW]
q'', q''_{CHF} = wall, critical heat flux [kW/m^2]
T_{sat}, T_{sub} = saturation and subcooled liquid temperature [K]
x_e = thermodynamic quality at the loop exit
y+ = dimensionless wall distance
z, z_0, z_1, z_{10} = interface level, steady, unsteady, initial [m]

Greek Letters

$\alpha, \bar{\alpha}, \alpha_{max}$ = void fraction, area-averaged, wall maximum
Δh = total enthalpy change [J/kg]
ϵ = small parameter
Λ = inertia grouping
ρ_l, ρ_v = liquid and vapor density [kg/m^3]
σ, σ_s = growth rate, Eq.(7) [1/s], and surface tension [N/m]
Φ_{lo}^2 = two-phase friction multiplier
ω, ω_n = oscillation and natural angular frequency [rad/s]

ACKNOWLEDGEMENTS

This work was supported by the Nuclear Safety Research Program through the Regulatory Research Management Agency for SMRs (RMAS) and the NSSC of the Republic of Korea (No. RS-2025-02309978).

REFERENCES

[1] S. G. Lim, H.S. Nam, D.H. Lee, S.W. Lee, Design characteristics of nuclear steam supply system and passive safety system for Innovative Small Modular Reactor (i-SMR). Nucl. Eng. Technol Vol. 57, 103697, 2025.
[2] J.A. Boure, A.E. Bergles, L.S. Tong, Review of two-phase flow instability, Nuclear Engineering and Design, Vol. 25, Issue 2, pp. 165-192, 1973.
[3] F. Inada, M. Furuya, A. Yasuo, Thermo-hydraulic instability of boiling natural circulation loop induced by flashing (analytical consideration). Nucl. Eng. Des. 200 (1–2), 187-199, 2000.
[4] M. Furuya, F. Inada, T.H.J.J. van der Hagen, Flashing-induced density wave oscillation in a natural circulation BWR-mechanism of instability and stability map. Nucl. Eng. Des. 235, 1557-1569, 2005.
[5] C. Tompkins, M. Corradini, Flow pattern transition instabilities in a natural circulation cooling facility, Nuclear Engineering and Design, Vol. 332, pp. 267-278, 2018.
[6] J.C. Jo, F.J. Moody, K.S. Do, Analytical Study of Flow Instability in a Natural Circulation Pressurized Water Reactor Auxiliary Feedwater System. ASME J.PVT, 137, 0245011-0245015, 2015.
[7] ANSYS Inc., ANSYS CFX-Solver Theory Guide, ANSYS Inc., Canonsburg, PA, USA (2021).
[8] J.C. Jo, H. Lee, Technical Guidelines for CFD Analysis in Validating Fuel Assembly CHF Test Results, Trans. KNS Spring Meeting, Jeju, Korea, May 7-8, 2026.
[9] Verma, G., Sinha, S. L., Verma, S. K., Verma, T. N. (2025). A Review of CFD Advancements Toward Thermal-Hydraulic Analysis of Prototypical Flow Conditions in PWR Subchannels. Nucl. Tech., 211(7), 1363–1406.
[10] Zhang, R., Cong, T., Su, S., Wang, J., Qiu, S. (2020). Investigation on the critical heat flux in typical 5 by 5 rod bundle at conditions prototypical of PWR based on CFD methodology. Applied Thermal Eng., 179, 115582.
[11] X. Fang, A. Dong, A comparative study of correlations of critical heat flux of pool boiling. *J. Nucl. Sci. Tech.*, *54*(1), 1–12, 2017.
[12] N. Zuber, J.A. Findlay, Average Volumetric Concentration in Two-Phase Flow Systems, ASME. *J. Heat Transfer*. 87(4): 453–468, November 1965.
[13] J.C. Jo, F.J. Moody, Simplified Analysis of Two-Phase Flow in a Passive Containment Cooling System, Trans. ANS Annual Conf., 810-813, May 3-June 3, 2026, Denver, CO, USA.